Strong piezoelectric response in layered CuInP₂S₆ nanosheets for piezoelectric nanogenerators

Weng Fu Io[1], Man-Chung Wong[1], Sin-Yi Pang[1], Yuqian Zhao[1], Ran Ding[1], Feng Guo[1], Jianhua Hao[1]*

[1] *Department of Applied Physics, The Hong Kong Polytechnic University, Hong Kong, P. R. China*

*Corresponding author.

E-mail address: jh.hao@polyu.edu.hk

Abstract

Piezoelectricity in two-dimensional (2D) materials have received particular attention because of their great potential in realizing nanoscale piezotronic devices. However, most 2D layered piezoelectric materials found so far possess only in-plane piezoelectricity and require the induction of stress by bending flexible substrate, which limits their integration with conventional rigid substrates such as silicon wafer. $CuInP_2S_6$ is a promising 2D layered material that has attracted widespread devotion due to its diverse excellent properties including out-of-plane ferroelectricity and high stability at room-temperature. However, comprehensive investigation of piezoelectric effect in 2D $CuInP_2S_6$ and its relevant piezoelectric device application is still at an initial stage compared to the extensive investigation of its ferroelectricity. Herein, we perform a quantitative analysis of the large out-of-plane piezoelectricity in multilayer $CuInP_2S_6$ and therefore demonstrate the device application for 2D piezoelectric nanogenerator (PENG). Few-layer $CuInP_2S_6$ nanosheet shows a high d_{33} piezoelectric coefficient of 17.4 pm/V, outperforming other 2D layered piezoelectrics currently reported. Moreover, the PENG based on a single $CuInP_2S_6$ nanoflake illustrates a maximum piezoelectric current and voltage responses of 1.7 nA and 12 mV, respectively. The experimental results are discussed based on the piezotronic effect. The strong piezoelectric response achieved in 2D $CuInP_2S_6$ nanosheets warrants their potential to be adopted for future strain-modulable nanoelectronic and piezotronic devices integrated with silicon-based chips.

Keywords

piezotronics, CuInP₂S₆ layers, out-of-plane piezoelectricity, piezoelectric nanogenerator

1. Introduction

Emerging two-dimensional (2D) van der Waals (vdW) layered materials, which possess multiple exceptional properties such as excellent carrier mobility and mechanical

flexibility compared to their bulk counterparts, show immense potential as multifunctional electronic materials in the coming nano era[1-3]. In recent years, extensive experimental and theoretical studies have been conducted, resulting in the discovery of many extraordinary phenomena in 2D layered materials including topological, photovoltaic, ferroelectric, piezoelectric and superconducting properties[4-11]. Among various functionalities, 2D materials possessing piezoelectricity widely employed for applications in energy harvesters, actuators, sensors, and piezoelectric field-effect transistors are relatively scarce. Due to the ultrathin dimension and the remarkable mechanical endurance against large strain, 2D piezoelectric materials are promising to be employed for nanoscale devices achieving high performance and low power consumption, motivating researchers to explore novel low-dimensional piezoelectric materials with strong electromechanical effects[12-22].

Since the discovery of 2D piezoelectricity in MoS_2 by Wang's group [18], theoretical calculations and experiments have been carried out to predict or observe piezoelectricity in atomically thin layers, such as monolayer transition metal dichalcogenides (TMDCs)[13, 17, 23], 2D wurtzite structures (ZnO, CdS, etc.) [24-27], monolayer group IV monochalcogenides[28], and Group-V binary compounds[29]. Unfortunately, the piezoelectric polarization in the new members of piezoelectric family is currently restricted to the in-plane direction, largely limiting their possibilities to be integrated into vertical nanoelectronic device systems. Moreover, most of the reported 2D layered piezoelectric materials exhibit layer-dependent piezoelectric properties. For instance, in-plane piezoelectricity only exists in the monolayer or few-layer TMDCs and declines in the piezo-polarization strength with increasing layer thickness[13, 15]; while some 2D materials possess odd-even-layer dependency in which the piezoelectric responses can only be observed in odd-layers[13, 30, 31]. Therefore, researchers have drawn great efforts in searching novel 2D layered materials with longitudinal piezoelectricity. Until now, out-of-plane piezoelectricity has been theoretically and experimentally reported in several 2D materials such as buckled group-III-V monolayers (d_{31}: 0.02 to 0.6 pm/V), Janus group-III chalcogenide monolayers (d_{31}: 0.07–0.46 pm/V), SnS_2 (d_{33}: 2.2-5 pm/V), 3R-MoS_2 (0.7-1.5 pm/V) and α-In_2Se_3 (d_{33}: 0.34-5.6 pm/V)[16, 20, 24, 32-35]. Nevertheless, their piezoelectric coefficients are rather small compared to the conventional out-of-plane piezoelectric perovskite materials, and therefore the discovery of more 2D vdW layered materials with robust piezoelectric effect is highly desired for the development of efficient nanoscale piezotronic devices.

Recently, a vdW layered material $CuInP_2S_6$ (CIPS) has been demonstrated to possess room-temperature ferroelectricity from bulk crystal to ultrathin samples of ~4 nm[36]. Through theoretical and experimental studies, You et al. revealed the origin of the

negative out-of-plane piezoelectricity in CIPS which is rarely observed in the piezoelectric family[37]. The piezoelectric and electrostriction coefficients of bulk CIPS single crystal was quantitatively measured to be much higher than that of most existing intrinsic layered piezoelectric materials. However, the piezoelectric effect of this vdW layered material when approaching the 2D limit has not been fully elucidated, and the potential applications in the nanoelectronics utilizing their piezoelectric properties still remain unexplored. Herein, we quantitatively and systemically evaluate the thickness-dependent large out-of-plane piezoelectric coefficients in 2D CIPS nanoflakes down to ~3.5 nm using the piezoresponse force microscopy (PFM) technique. More importantly, the piezotronic effect in CIPS nanoflakes is demonstrated under compressive stresses and we explore the investigation of 2D CIPS-based vertical piezoelectric nanogenerators and evaluate their device performances towards practical piezoelectric applications, which is not yet addressed in earlier studies. Our work reveals the strong longitudinal piezoelectricity in 2D CIPS nanoflakes and its great potential in nanoscale piezotronic and energy harvesting applications on rigid substrates such as Si wafer.

2. Material and methods

2.1 Material preparation and characterizations

Bulk CIPS and α-In$_2$Se$_3$ single crystals were purchased from 2D Semiconductors USA and HQ Graphene company, respectively. Ultrathin films were fabricated by mechanical exfoliation with scotch tape onto arbitrary substrates. The Raman spectra were measured using an excitation laser with 532 nm wavelength and 1 μm spot size (Witec Confocal Raman system). The high-resolution transmission electron microscope (HRTEM) image, selected area electron diffraction (SAED) pattern and the mapping performed in scanning transmission electron microscopy (STEM) were investigated using JEOL 2100F Transmission Electron Microscope device with an accelerating voltage of 200 kV equipped with an energy-dispersive X-ray (EDX) spectrometer system and the exposure time for acquiring an image is 0.5 s. Powder X-ray diffraction (XRD) was performed with Rigaku smart lab 9 kW (Rigaku, Japan) linked to a 2D detector with Cu K radiation (λ = 0.154 nm). The second-harmonic generation (SHG) spectrum was obtained under an excitation wavelength of 900 nm using Leica TCS SP8 MP confocal microscopy. The PFM measurements were investigated by Asylum MFP-3D Infinity in dual ac resonance tracking piezo force microscopy (DART-PFM) mode. A conductive probe with Pt/Ir coating and a force constant of 2.8 N/m was employed in all PFM characterizations and an ac bias V_{ac} in the range of 1-4 V was applied during the ferroelectric and piezoelectric measurements.

2.2 Device fabrication and electrical characterization

For the construction of CIPS-based devices in this work, an array of electrodes was first prepared by patterning 50-nm Au electrodes via standard photolithography followed by electron-beam (E-beam) evaporation of metal. Next, CIPS nanosheets were mechanically exfoliated from their parent bulk crystal. Ultrathin CIPS samples were chosen, aligned under optical microscopy, and laminated onto pre-deposited Au electrodes on insulating SiO_2/Si substrates through a dry transfer technique. Finally, another as-fabricated 50-nm Au electrode was physically peeled off, aligned, and transferred on top of the CIPS/Au junctions by vdW integration. The piezotronic effect measurements were performed using a probe station equipped with Keithley 4200-SCS semiconductor parameter analyzer. Here, for the fabrication of the CIPS piezoelectric nanogenerator (PENG), ultrathin CIPS nanoflakes with the thickness of 20-60 nm and lateral size of 15-30 μm were selected. Next, silver paste was painted on the electrodes to connect the conductive wires with the nanoscale CIPS devices, and then a thin PMMA layer was drop-casted onto the fabricated PENG to encapsulate the device.

2.3 Piezoelectric output measurements

A home-built experimental setup was employed to investigate the piezoelectric outputs of the CIPS-based PENG devices. The tested PENG was fixed on a sample holder. A fine and rigid steel rod was mounted to a linear motor fixed on a 3D positioning stage to apply constant and periodic compressive forces on the PENG devices. A 600 MHz oscilloscope (LeCroy WaveSurfer 62Xs) and a low-noise current preamplifier (Stanford Research Systems, Model SR570) with a 3 Hz low-pass filter were employed to measure the outputs of piezoelectric voltage and current from the CIPS PENGs.

3. Results and discussion

In this study, CIPS nanosheets were prepared through mechanical exfoliation from their parent bulk crystal onto arbitrary substrates. Raman spectroscopy, XRD, TEM and EDX are adopted to characterize the structure and quality of the CIPS crystal. The XRD spectrum (Supplementary Figure S1) obtained at room temperature displays two strong and sharp peaks at 13.9° and 27.8° which are assigned to (002) and (004) planes, respectively, which is in good agreement with the reported ferroelectric phase CIPS[38]. Figure 1(a) shows the atomic structure for the side and top views of CIPS, illustrating its non-centrosymmetric structure. SHG microscopy was employed to verify the symmetry of the CIPS crystal. The strong SHG signal (Figure 1(b)) observed in CIPS nanoflakes indicates the structural centro-symmetry lacking which is relevant to the origins of the out-of-plane ferroelectricity and piezoelectricity in CIPS. Raman spectroscopy was applied to effectively identify and confirm the phase of the CIPS crystal at room temperature and the Raman spectra of CIPS nanoflakes with the thickness from 15 to 28 nm are demonstrated in Figure 1(c). The locations of the Raman

peaks of the exfoliated CIPS nanoflakes are consistent with previously reported vibration modes of bulk CIPS crystal at the ferroelectric phase[38]. The numerous broad peaks in the 60-80 and 300-325 cm^{-1} ranges correspond to the cation (Cu^{+}, In^{3+}) oscillation modes, and those in the 90-120 cm^{-1} range are ascribed to the oscillation modes of anion (P$_2$S$_6^{4-}$). The peaks in the 145-285 cm^{-1} range are attributed to the S-P-P and S-P-S stretching, and the P-P stretching is accountable for the sharp Raman peak at 375 cm^{-1}. Besides, Figure 1(d) presents the HRTEM image of CIPS thin film showing the crystal structure at atomic scale with uniform and periodic crystal lattices along identical orientation. The SAED pattern (inset of Figure 1(d)) illustrates multiple sets of rotational symmetry patterns with perfect hexagonal structure, indicating the high-quality and crystallinity of the CIPS crystal utilized in this work.
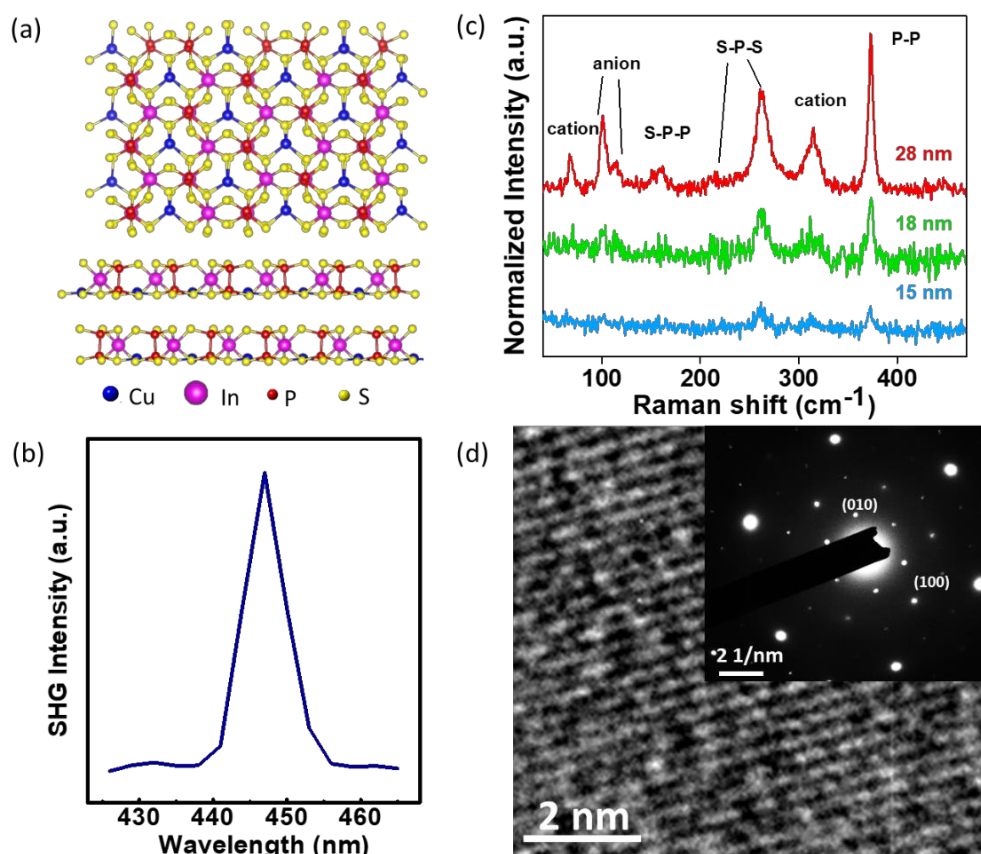

Figure 1. Structural characterizations of CIPS nanosheets. (a) Atomic structures for the top and side and top views of the non-centrosymmetric CIPS crystal. (b) SHG signal of CIPS samples at room temperature, with an excitation laser wavelength of 900 nm. (c) Raman spectra of CIPS nanoflakes measured at different thicknesses by using 532 nm excitation laser. (d) High-resolution TEM image of CIPS nanoflakes. Inset illustrates the corresponding SAED pattern.

To verify the out-of-plane piezoelectricity and ferroelectric polarization, we exfoliated ultrathin CIPS nanoflakes onto a conductive Pt substrate and tested them using PFM. The typical off-field PFM amplitude and phase hysteresis loops are as shown in Supplementary Figure S3, illustrating distinct butterfly-shaped amplitude loops and 180° switching between two discrete polarization states, which are typical features of ferroelectric materials. The polarization reversal was also demonstrated by applying a DC tip bias on the CIPS nanoflakes to modulate the ferroelectric domain pattern, and the initial and modified out-of-plane phase and amplitude patterns are shown in Supplementary Figure S4. In order to further characterize the fundamental piezoelectric properties of CIPS, ultrathin CIPS nanoflakes were exfoliated onto insulating SiO_2 surface to minimize the possible non-piezoelectric influences between the PFM probe and substrate. Figures 2(a) and (b) illustrate the topography and phase images of exfoliated CIPS nanoflakes with different thicknesses ranging from 3.5 to 20 nm. The out-of-plane amplitude and phase profiles of the CIPS nanoflakes are recorded under varied drive voltages from 1 V to 4 V, as shown in Figure 2(c) and Supplementary Figure S5, respectively, in which clear and obvious amplitude and phase contrasts can always be observed. Strong electromechanical responses can still persist even down to 3.5 nm (corresponds to ~5 layers of CIPS), and the PFM amplitude signal increases gradually when the voltage applied on the CIPS nanoflakes increases, indicating the existence of robust intrinsic out-of-plane piezoelectricity in ultrathin CIPS samples. Here, the CIPS nanoflakes with various thicknesses induce different magnitude of electromechanical signals that decline with reducing sample thickness. It indicates that this tendency of decrease in the piezoresponse with respect to the reduced sample thickness below 100 nm should be attributed to the intensified effect of depolarization field as well as the enhanced substrate clamping effect in ultrathin vdW layered ferroelectrics, as similar phenomena are often observable in many traditional and novel vdW layered ferroelectric and piezoelectric materials[16, 39, 40]. The schematic of the PFM technique for determining the piezoelectric effect is displayed in Supplementary Figure S6(a). As depicted in Supplementary Figure 6(b), the deflection signal of the conductive atomic force microscopy (AFM) tip increases proportionally with the driving voltage, hence the piezoelectric coefficient of the CIPS samples can be derived from the relationship between the piezoelectric amplitude and the applied voltage. The d_{33} piezoelectric coefficient of 2D CIPS nanoflakes is plotted as a function of the sample's thickness in Figure 2(d). A high d_{33} coefficient of 17.4 pm/V is quantitatively deduced in 3.5-nm-thick CIPS, which gradually increases with an increase in sample thickness and enhances to 83 pm/V when the thickness reaches up to 82 nm. The observed piezoelectric response is in good agreement to previous literature and outperforms most of the 2D layered piezoelectric materials previous reported, as listed

in Table S1 [12, 16, 20, 34, 35, 41]. In conventional three-dimensional piezoelectrics, the sign of piezoelectric coefficient is usually positive and the generated electric polarization will always increase in response to a tensile strain. The piezoelectric coefficient can be divided into the clamped-ion and internal-strain terms[42]. For low-dimensional vdW layered piezoelectric materials, the internal-strain term is greatly suppressed owing to the much weaker and softer interlayer vdW interactions than the intralayer chemical bonding. Moreover, due to the "lag of Wannier center" effect[43], the clamped-ion term is usually negative in layered low-dimensional piezoelectrics. In low-dimensional layered CIPS, the interlayer vdW gap accounts for the majority of the change in dimension under external stress, while the intralayer thickness and the associated dipole only change barely. For CIPS, the internal-strain contribution to piezoelectricity is too small to offset the negative clamped-ion term, giving rise to the negative piezoelectricity in CIPS[43]. Hence, the electric polarization in CIPS is more likely to increase when a compressive stress is applied. On the other hand, large out-of-plane piezoelectric magnitude in ultrathin CIPS nanoflakes mainly originates from the weak interlayer vdW interactions combined with the high displacive instability of Cu atoms across the vdW gap, as revealed in previous studies[37, 43, 44]. At room temperature, the thermal energy is sufficient to overcome the small energy barrier for the Cu atoms to hop between interlayer sites. Under compressive stress, the soft vdW gap takes most of the change in dimension, and the hopping motion of the Cu atoms between interlayer sites will also increase. With a higher occupancy of Cu in the interlayer site, the electric polarization of CIPS is also enhanced, thus resulting in the strong piezoelectric responses of CIPS. For a direct and reliable comparison, we also quantitatively estimated the piezoelectric coefficient of α-In$_2$Se$_3$ which is a well-studied 2D vdW layered ferroelectric and piezoelectric semiconductor, under identical measurement conditions using our test system (Supplementary Figure S7). The derived piezoelectric magnitude of few-layer CIPS in this work is around 30 times larger than that of few-layer α-In$_2$Se$_3$ (~0.53 pm/V) and almost 6 times larger for thicker nanoflakes. According to the previous theoretical and experimental works on the piezoelectricity of CIPS and α-In$_2$Se$_3$, the d_{33} piezoelectric coefficient of CIPS bulk crystal is much higher than that of bulk α-In$_2$Se$_3$ single crystal[16, 44-46]. Our result accords with the previous reports. The large difference in the magnitude of the piezoelectric coefficient is due to the difference in the crystal structures of the two vdW layered piezoelectric materials. Both the α-In$_2$Se$_3$ and CIPS possess an intrinsic non-centrosymmetric crystal structure. In α-In$_2$Se$_3$, the out-of-plane piezoelectricity originates from the off-centering Se atoms forming electric dipoles, while the intralayer atoms are stably connected together by strong chemical bonding. In comparison, the piezoelectricity in CIPS is mainly contributed by the Cu atoms in which the high unstable displacement of Cu atoms

greatly enhances the electric polarization under stress, resulting in a much larger magnitude of d_{33} piezoelectric coefficient than that of α-In$_2$Se$_3$ at the same thickness. Moreover, from the technological perspective, the experimental d_{33} coefficient of ultrathin CIPS is comparable to those high-performance inorganic piezoelectric thin films[21, 37, 47, 48], making it a desirable candidate material for evolving piezotronic nanotechnology.
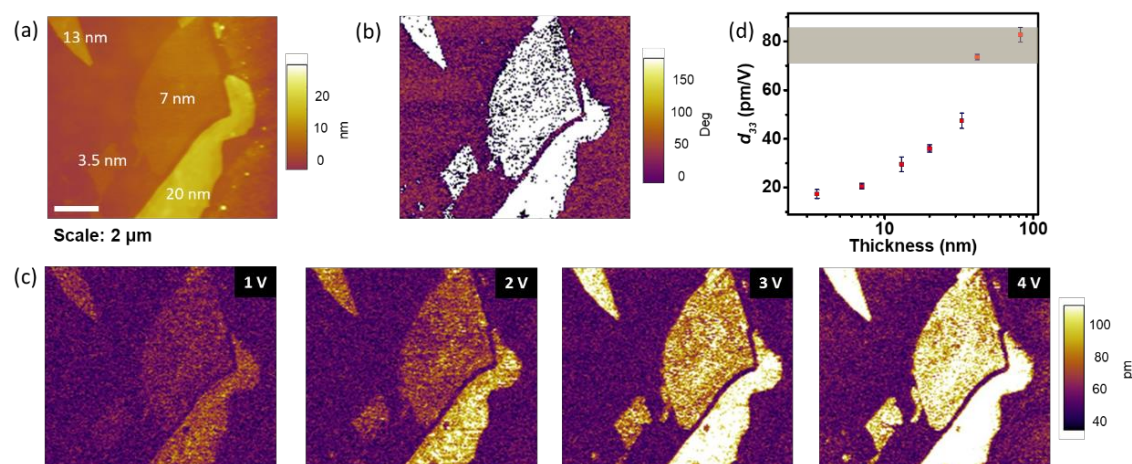
Figure 2. Out-of-plane piezoelectric responses of CIPS samples. (a-b) AFM and PFM phase images of CIPS nanoflakes exfoliated onto SiO$_2$ substrate. (c) PFM amplitude images of CIPS nanoflakes measured under different AC voltages. (d) Dependence of the d_{33} piezoelectric coefficient with respect to the nanoflake thickness (<100 nm).

The vdW piezoelectrics own remarkable merits beyond perovskite oxide-based counterparts in the future innovation of miniatured devices. So far, most of the conventional perovskite oxide materials are with poor complementary compatibility of metal-oxide-semiconductor structure when the thickness approaching the 2D limit and necessarily be fabricated on certain specific substrates or through specific synthesis approaches, limiting their potential for effective ultrathin 2D piezoelectric device applications[49]. In stark contrast to the oxide-based piezoelectrics, 2D vdW piezoelectrics-based nanodevices are highly compatible with various substrates such as silicon and polymers, while their intrinsic piezoelectric properties can sufficiently be retained. In this work, the CIPS-based nanodevices were constructed on silicon substrates, demonstrating their excellent compatibility with traditional semiconductor industry. Taking advantage of the strong out-of-plane piezoelectricity of CIPS nanoflakes, we first studied the room-temperature transfer characteristic of the CIPS-based devices to explore the potential applications. The basic structure of the piezotronic devices is consisted of two Schottky contacts (Au-CIPS interfaces) and one semiconducting channel (CIPS nanoflakes). To fabricate the CIPS-based devices, we

prepared a series of electrodes onto Si substrates through standard photolithography and E-beam evaporation, which could be physically picked up and transferred onto arbitrary surfaces while maintaining atomically flat surfaces (see details in experimental section and Supplementary Figure S8). Sequentially, mechanically exfoliated ultrathin CIPS film with appropriate thickness was transferred to the top of the pre-fabricated metal electrode on SiO_2/Si substrate. Finally, another pre-deposited metal electrode was physically exfoliated, aligned, and laminated on the top of the CIPS/metal junction under optical microscope through the dry transfer technique, forming precise and clean vdW metal-semiconductor contact.
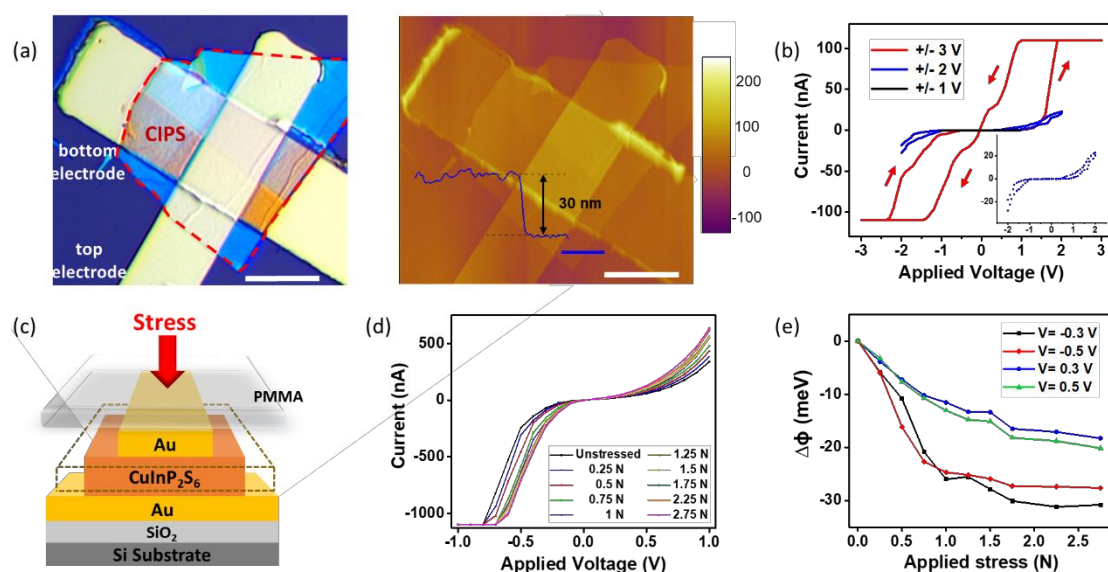

Figure 3. Piezotronics effect in CIPS devices. (a) The optical image (left), corresponding AFM image and height profile (right) of a typical CIPS device with symmetric top and bottom Au electrodes and an active area of ~120 μm^2. Scale: 10 μm. (b) Typical electrical characteristics of the ferroelectric CIPS when the applied voltage $V<V_c$ (Schottky junction behaviors) and $V>V_c$ (resistive switching behaviors). Inset: enlarged *I-V* curve (blue). (c) Schematic illustration of CIPS-based piezotronics device covered by a thin layer of PMMA under compressive stress. (d) $I-V$ electrical characteristics the CIPS device under different levels of compressive stress. (e) The calculated change in barrier height as a function of the applied compressive force at an external voltage of +/- 0.3 and +/- 0.5 V, respectively.

The approach to constructing metal-semiconductor junction devices with pre-fabricated and mechanically transferred metal electrodes is advantageous over that with direct deposition of metal electrodes on the top of the 2D semiconducting materials. For instance, the conventional metal evaporation process through direct chemical bonding would usually generate defects, trapped states, and polymer residues at the metal-

semiconductor interface, resulting in the pinning of the Fermi level, changing of the band structures, Schottky barrier height, and the charge transfer characteristics[50]. Moreover, the high-energy metal bombardment during the evaporation process could cause degradation even damage to the crystal structure of the 2D materials. Particularly for the vertical device structures utilized in this work, the diffusion of metal into the underlying CIPS nanoflakes might even penetrate through the nanoscale semiconducting channel and contact with the bottom electrode during electrical characterization of the devices, leading to a short circuit. On the contrary, the vdW integration is a facile and non-destructive approach to physically assemble metal electrodes on 2D materials for device fabrication. As direct chemical deposition process is avoided, the correlated interfacial defects, trap states, and metal diffusion can be prevented, thus preserving the crystal lattice and material properties of the 2D semiconductors and the effect of Fermi level pinning can be reduced sufficiently. Figure 3(a) displays the optical and AFM images of a representative vertical piezotronic device with a 30-nm-thick CIPS nanoflake as the channel and an active area of ~120 μm^2. The optical microscopy images of several fabricated CIPS-based devices in Supplementary Figure S9 illustrate that mechanically laminated top metal electrodes can still retain their smooth and flat surfaces. Figure 3(b) presents the *I-V* characteristics of the CIPS device under unstressed condition. When the external voltage is below the coercive voltage (V_c), typical Schottky contact behavior is demonstrated. It implies that the two vertical metal-semiconductor junctions form good Schottky contacts, which are beneficial for further electrical measurements. When the applied voltage $V > V_c$, the representative resistance switching phenomenon of the ferroelectric CIPS is illustrated in the *I-V* curve, while the large hysteresis loop suggests that the two resistance states are resulted from the reversal of the ferroelectric polarization directions rather than from the mobility of defects and/or residues introduced during the vdW assembly process. Moreover, the piezoelectric-modulated electrical transfer characteristic of the CIPS-based devices under different mechanical stresses were investigated. As schematically presented in Figure 3(c), the fabricated metal-semiconductor-metal (M-S-M)-structured devices are packaged by a thin layer of polymethylmethacrylate (PMMA). With this configuration, the external mechanical stress can be evenly applied to the entire active area of the CIPS nanoflake and the piezoelectric polarization charges be well distributed on the sample surfaces. The piezo-induced electrical responses of the CIPS-based devices are examined under vertically applied compressive force varying from 0.25 N to 2.75 N with a small voltage ($V \ll V_c$) so that the ferroelectric domain configuration in CIPS would not be modified by the applied mechanical stress and external bias. Note that the maximum measurable output current is restricted to 1.1 μA to avoid excess current flowing through the ultrathin 2D semiconducting channel

and destroying the CIPS piezotronic devices. The output current in both forward and reverse conditions are modulable by stress, with an obvious increasing trend in the current magnitudes. The current increases from 243.3 nA to 704.7 nA upon 1.75 N compressive force and an external voltage of -0.5 V, and tends to saturate with larger compressive force (Figures 3(d) and Supplementary Figure S10(a)). The stress-induced Schottky barrier height change ($\Delta\Phi$) is quantitatively estimated according to the experimental data from in Figure 3(d) (see calculation details in Supporting Information).The results are plotted in Figure 3(e) at two fixed voltages of +/- 0.3 V and +/- 0.5 V, showing that the barrier heights at the source and drain contacts are both reduced when increasing compressive stress. Moreover, the change in the Schottky barrier height is fairly consistent under different bias, indicating that the variation in barrier height is not apparently affected by the voltage applied to the piezotronic device. The stress-induced variation in the electrical properties of the CIPS-based junction devices is consistent with the piezotronic effect previously reported in other 2D piezoelectric semiconductors, where the applied mechanical stimulus functions as a "gate" to tune the carrier transport processes in piezotronic devices[8, 51].
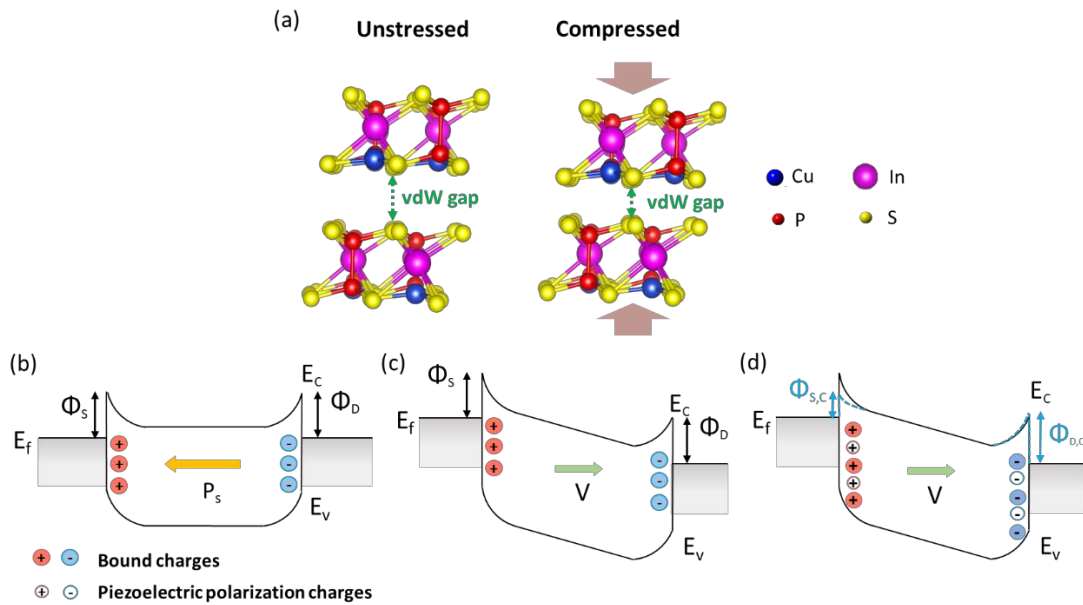

Figure 4. (a) Side view of the bilayer CIPS crystal structure in the unstressed and compressed conditions. Band diagrams under different conditions: (b) zero applied stress with zero external bias. (c) Zero stress with nonzero external bias resulting in the tilting of the energy band. (d) Compressive stress applied with nonzero external bias leading to piezopotential generated at the two interfaces. Φ_S and Φ_D indicate the initial Schottky barrier heights at the source and drain contacts, respectively. $\Phi_{S,C}$ and $\Phi_{D,C}$ are the modified Schottky barrier heights at the source and drain contacts modified by piezoelectric polarization charges.

The phenomenon observed in CIPS nanosheets can be understood based on the piezotronic effect[52-54]. The crystal structures and energy band diagrams under different conditions are proposed in Figure 4. Without applying stress and external bias, the spontaneous ferroelectric bound polarization charges reside at the two surfaces of the CIPS flake (Figure 4(b)). Upon application of stress, piezoelectric polarization charges are generated at the CIPS surfaces which can regulate the metal-semiconductor interfaces, and the piezopotential created under applied stress is able to modify the Schottky barrier heights. Under the application of a small electric voltage ($V \ll V_c$) at unstressed condition, the energy band of the semiconducting CIPS is tilted as indicated in Figure 4(c). When a compressive stress is applied under a small external voltage, piezoelectric polarization charges generated at the two interfaces changes the Schottky barrier heights, resulting in enhanced electrical outputs. The generated positive piezo-polarization charges would induce positive piezopotential, hence lowering the Schottky barrier at the semiconductor-metal interface. While negative piezo-polarization charges and the created negative piezopotential lead to an increase in the barrier height, as shown in Figure 4(d). The changes in the energy bands at the two metal-semiconductor interfaces are asymmetric and cause modification on the charge transport. Accordingly, the current can be manipulated by utilizing the generated piezopotential as a gating source. In this work, we have fabricated and investigated the piezotronic performance of more than 20 two-terminal CIPS nanodevices, and most showed similar transfer characteristic with robust room-temperature piezotronic effect, demonstrating a high reliability and repeatability of the result and offering great possibilities for CIPS to exploit in nanoscale energy harvesting applications.

To expand the investigation of the piezotronic effect in 2D CIPS and further demonstrate its potential applications, we prepared CIPS-based piezoelectric nanogenerators and examined their performances. The piezoelectric responses from the CIPS PENG, in which the piezoelectric CIPS nanoflake is sandwiched between two Au electrodes on SiO_2/Si substrate, were measured under constant vertical periodic compression and release actions, and the schematic of the home-made experimental system for mechanical force application is displayed in Figure 5(a). The current density can be promoted when thinner CIPS samples are used, however, the suppression effect of the depolarization field on the polarization strength is also enhanced. Hence, the thickness of the CIPS nanoflakes used for constructing the nanogenerators was controlled in the range of ~20-50 nm, with an energy harvesting active area in the range of 100-140 μm^2. Upon compressive stress, piezo-polarized charges were produced at the two surfaces of the CIPS nanoflakes and modulated the barrier height on the metal-semiconductor interfaces, resulting in an electrical output peak. When the mechanical force was released, the piezoelectric polarization charges with opposite signs were

generated, and an electrical signal in a reverse direction would be obtained. The corresponding piezoelectric voltage and current outputs repeatedly generated from the periodic compressive and release forces are shown in Figures 5(b)-(c), and Supplementary Figures S12(a)-(b). The output piezoelectric voltage and the piezoelectric current of a typical CIPS PENG device (thickness of ~45 nm) are about ~8 mV and 1.15 nA, respectively. When a thinner CIPS nanoflake of ~15 nm is employed in the PENG device, the piezoelectric peak voltage and the current outputs increase to 12 mV and 1.7 nA, respectively, indicating the excellent piezoelectric properties of 2D CIPS nanoflakes. The piezoelectric current outputs were examined with a series of external load resistances (see Supplementary Figure S12(d) for the circuit connection detail) in order to quantify the output power of the CIPS nanogenerators. The current outputs and power density as a function of the used load resistances are presented in Figure 5(d). The piezoelectric peak current is relatively constant when the loading resistance is below 10 MΩ, then it begins to drop dominantly when increasing external load resistance. The effective energy harvesting area of the tested single CIPS nanoflake was ~120 μm^2, and the maximum power density was estimated to be around 70.4 nW/cm^2 with a load resistance of 100 MΩ. Figure 5(e) displays the piezoelectric current responses of the PENG device with various applied stress. The magnitude of the piezoelectric current enhances with increasing stress, demonstrating the typical out-of-plane piezoelectric characteristics of CIPS nanoflakes. Furthermore, we tested the piezoelectric output stability and mechanical durability by applying continuous and cycled compressive stress to the CIPS nanogenerator over a long operation time of longer than 1200 seconds. For the entire testing period, the measured voltage outputs are almost consistent in magnitude with no obvious variations observed, denoting the good stability of the output piezoelectric signals and the good mechanical durability of the CIPS-based PENG device (Figure 5(f)). In addition, a connection polarity switching test was carried out to validate that the electrical outputs were originated from the piezoelectric effect in CIPS, rather than the contributions from other non-piezoelectric factors such as the testing instruments. The voltage output signals from the CIPS PENG are presented in Supplementary Figure S13, indicating that the output voltage direction is switchable as expected when the connection polarity is reversed. Owing to the vertical structure of the CIPS PENG, the piezoelectric channel length is determined only by the thickness of the CIPS nanoflakes utilized in the devices. The nanoscale channel length leads to a high output piezoelectric current in the CIPS PENG devices, which is one to two orders of magnitude larger than that of the reported 2D in-plane PENGs based on single nanoflake including TMDCs (MoS$_2$ and WSe$_2$)[15, 17, 19] and layered metal dichalcogenide[35]. On the other hand, the piezoelectric voltage output of the out-of-plane CIPS PENG is also comparable to that of other 2D

in-plane PENGs. These results demonstrate that 2D CIPS nanoflakes hold great potential to be adopted in nanoscale high-performance energy harvesting applications.
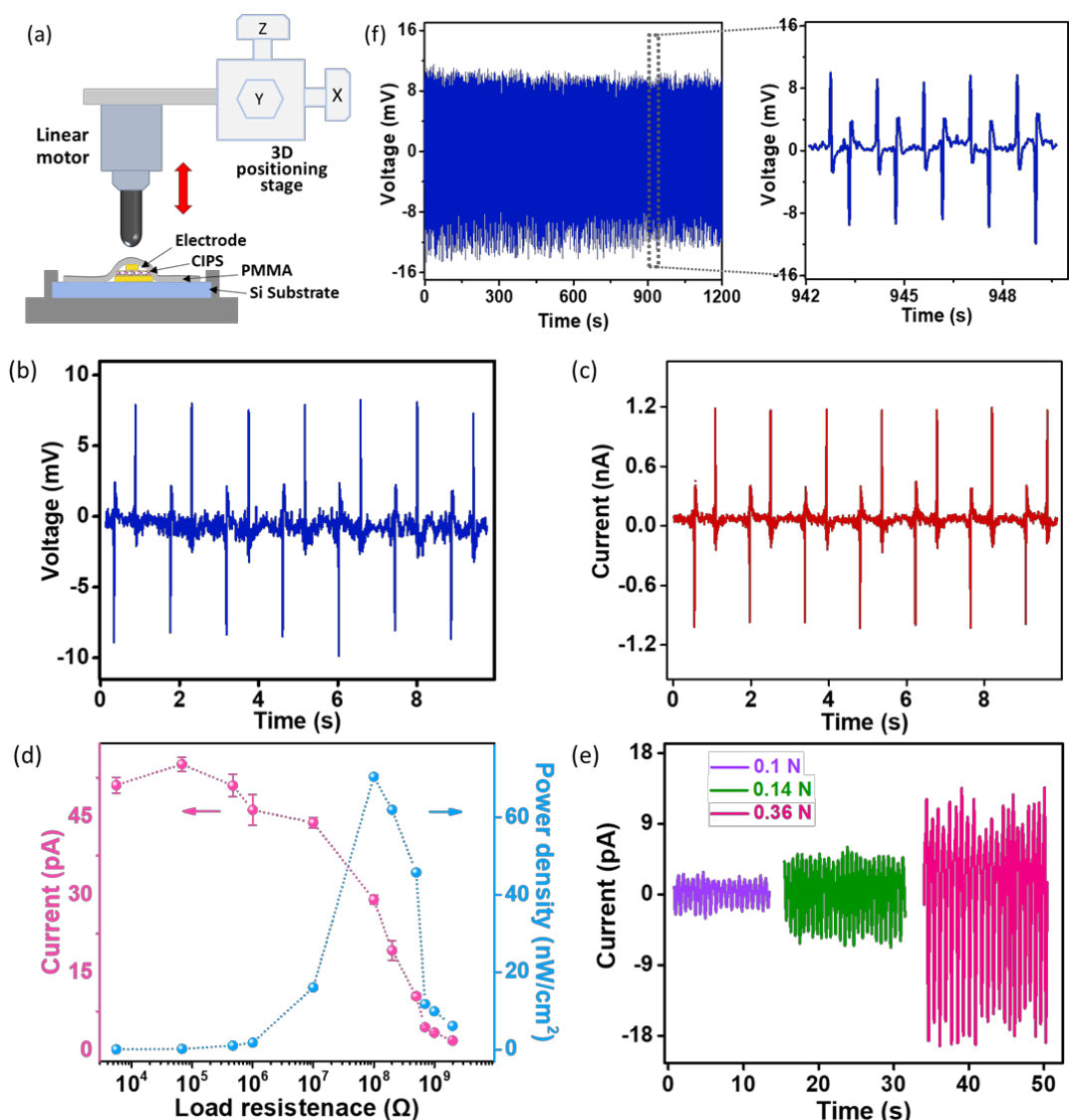
Figure 5. Electrical outputs from multilayer CIPS piezoelectric nanogenerators. (a) Schematic of the experimental setup for 2D CIPS PENG measurements in this work. The output (b) voltage and (c) current of a typical CIPS PENG generated by periodical longitudinal compression. (d) The peak close-circuit piezoelectric output current and corresponding power density of a CIPS PENG device under different external loading resistances. (e) Piezoelectric current responses under various compressive stress. (f) Durability test result of CIPS PENG.

4. Conclusion

In conclusion, we quantitatively investigate the layer-dependent out-of-plane piezoelectric response of CIPS nanosheets in the 2D regime and show the piezotronic

effect in CIPS-based devices. By using PFM, the vertical piezoelectric signals of the nanosheets enhance significantly when increasing sample's thickness. Specifically, the piezoelectric coefficient d_{33} for few-layer CIPS is 17.4 pm/V, which is larger than that reported from other currently explored 2D vdW piezoelectric materials. Furthermore, we fabricate 2D CIPS-based PENG through a facile and non-destructive vdW integration approach. The output piezoelectric current and voltage of the nanogenerator under uniform compression reach a maximum value of 1.7 nA and 12 mV respectively, while the peak power density reaches 70.4 nW/cm^2. The strong out-of-plane piezoelectricity in ultrathin CIPS endow them with superior opportunities to be integrated into nanoscale energy storage and conversion devices, as well as piezotronic devices.

Acknowledgements

Appendix A. Supporting information

References

[1]   C. Lee, X. Wei, J.W. Kysar, J. Hone, Measurement of the elastic properties and intrinsic strength of monolayer graphene, Science 321 (2008) 385-388.

[2]   F. Xia, T. Mueller, Y.M. Lin, A. Valdes-Garcia, P. Avouris, Ultrafast graphene photodetector, Nat. Nanotechnol. 4 (2009) 839-843.

[3]   K.I. Bolotin, K.J. Sikes, Z. Jiang, M. Klima, G. Fudenberg, J. Hone, P. Kim, H.L. Stormer, Ultrahigh electron mobility in suspended graphene, Solid State Commun. 146 (2008) 351-355.

[4]   Z. Yang, J. Hao, Recent progress in 2D layered III–VI semiconductors and their heterostructures for optoelectronic device applications, Adv. Mater. Technol. 4 (2019) 1900108.

[5]   S. Yuan, X. Luo, H.L. Chan, C. Xiao, Y. Dai, M. Xie, J. Hao, Room-temperature ferroelectricity in MoTe$_2$ down to the atomic monolayer limit, Nat. Commun. 10 (2019) 1-6.

[6]   L. Niu, F. Liu, Q. Zeng, X. Zhu, Y. Wang, P. Yu, J. Shi, J. Lin, J. Zhou, Q. Fu, W. Zhou, T. Yu, X. Liu, Z. Liu, Controlled synthesis and room-temperature pyroelectricity of CuInP$_2$S$_6$ ultrathin flakes, Nano energy 58 (2019) 596-603.

[7]   M. Si, P.-Y. Liao, G. Qiu, Y. Duan, P.D. Ye, Ferroelectric field-effect transistors based on MoS$_2$ and CuInP$_2$S$_6$ two-dimensional van der Waals heterostructure, ACS Nano 12 (2018) 6700-6705.

[8]   R. Ding, Y. Lyu, Z. Wu, F. Guo, W.F. Io, S.Y. Pang, Y. Zhao, J. Mao, M.C. Wong, J. Hao, Effective piezo- phototronic enhancement of flexible photodetectors based on 2D hybrid perovskite ferroelectric single- crystalline thin- films, Adv. Mater. 33 (2021) 2101263.

[9]   F. Guo, M. Song, M.C. Wong, R. Ding, W.F. Io, S.Y. Pang, W. Jie, J. Hao, Multifunctional optoelectronic synapse based on ferroelectric van der Waals heterostructure for emulating the entire human visual system, Adv. Funct. Mater. 32 (2022) 2108014.

[10]   W.F. Io, S. Yuan, S.Y. Pang, L.W. Wong, J. Zhao, J. Hao, Temperature- and thickness-dependence of robust out-of-plane ferroelectricity in CVD grown ultrathin van der Waals α-In_2Se_3 layers, Nano Res. 13 (2020) 1897-1902.

[11]   A.A. Balandin, S. Ghosh, W. Bao, I. Calizo, D. Teweldebrhan, F. Miao, C.N. Lau, Superior thermal conductivity of single-layer graphene, Nano Lett. 8 (2008) 902-907.

[12]   V.A. Cao, M. Kim, W. Hu, S. Lee, S. Youn, J. Chang, H.S. Chang, J. Nah, Enhanced piezoelectric output performance of the SnS2/SnS heterostructure thin-film piezoelectric nanogenerator realized by atomic layer deposition, ACS Nano 15 (2021) 10428-10436.

[13]   W. Wu, L. Wang, Y. Li, F. Zhang, L. Lin, S. Niu, D. Chenet, X. Zhang, Y. Hao, T.F. Heinz, J. Hone, Z.L. Wang, Piezoelectricity of single-atomic-layer MoS_2 for energy conversion and piezotronics, Nature 514 (2014) 470-474.

[14]   P. Li, Z. Zhang, W. Shen, C. Hu, W. Shen, D. Zhang, A self-powered 2D-material sensor unit driven by a SnSe piezoelectric nanogenerator, J. Mater. Chem. A 9 (2021) 4716-4723.

[15]   S.K. Kim, R. Bhatia, T.-H. Kim, D. Seol, J.H. Kim, H. Kim, W. Seung, Y. Kim, Y.H. Lee, S.-W. Kim, Directional dependent piezoelectric effect in CVD grown monolayer MoS_2 for flexible piezoelectric nanogenerators, Nano energy 22 (2016) 483-489.

[16]   F. Xue, J. Zhang, W. Hu, W.-T. Hsu, A. Han, S.-F. Leung, J.-K. Huang, Y. Wan, S. Liu, J. Zhang, J.-H. He, W.-H. Chang, Z.L. Wang, X. Zhang, L.-J. Li, Multidirection piezoelectricity in mono- and multilayered hexagonal α- In_2Se_3, ACS Nano 12 (2018) 4976-4983.

[17]   S.A. Han, T.H. Kim, S.K. Kim, K.H. Lee, H.J. Park, J.H. Lee, S.W. Kim, Point-defect- passivated MoS_2 nanosheet- based high performance piezoelectric nanogenerator, Adv. Mater. 30 (2018) 1800342.

[18]   X. Cui, Q. Xu, X. Ni, Y. Zhang, Y. Qin, Atomic-thick 2D MoS2/insulator interjection structures for enhancing nanogenerator output, J. Mater. Chem. C 6 (2018) 899-96.

[19] J.H. Lee, J.Y. Park, E.B. Cho, T.Y. Kim, S.A. Han, T.H. Kim, Y. Liu, S.K. Kim, C.J. Roh, H.J. Yoon, H. Ryu, W. Seung, J.S. Lee, J. Lee, S.W. Kim, Reliable piezoelectricity in bilayer WSe_2 for piezoelectric nanogenerators, Adv. Mater. 29 (2017) 1606667.

[20] H. Hallil, W. Cai, K. Zhang, P. Yu, S. Liu, R. Xu, C. Zhu, Q. Xiong, Z. Liu, Q. Zhang, Strong piezoelectricity in 3R‐ MoS_2 flakes, Adv. Electron. Mater. (2022) 2101131.

[21] S. Yuan, W.F. Io, J. Mao, Y. Chen, X. Luo, J. Hao, Enhanced piezoelectric response of layered In_2Se_3/MoS_2 nanosheet-based van der Waals heterostructures, ACS Appl. Nano Mater. 3 (2020) 11979-11986.

[22] W. Ma, J. Lu, B. Wan, D. Peng, Q. Xu, G. Hu, Y. Peng, C. Pan, Z.L. Wang, Piezoelectricity in multilayer black phosphorus for piezotronics and nanogenerators, Adv. Mater. 32 (2020) e1905795.

[23] K.-A.N. Duerloo, M.T. Ong, E.J. Reed, Intrinsic piezoelectricity in two-dimensional materials, J. Phys. Chem. Lett. 3 (2012) 2871-2876.

[24] M.N. Blonsky, H.L. Zhuang, A.K. Singh, R.G. Hennig, Ab Initio prediction of piezoelectricity in two-dimensional materials, ACS Nano 9 (2015) 9885-9891.

[25] L. Wang, S. Liu, Z. Zhang, X. Feng, L. Zhu, H. Guo, W. Ding, L. Chen, Y. Qin, Z.L. Wang, 2D piezotronics in atomically thin zinc oxide sheets: Interfacing gating and channel width gating, Nano energy 60 (2019) 724-733.

[26] L. Wang, S. Liu, G. Gao, Y. Pang, X. Yin, X. Feng, L. Zhu, Y. Bai, L. Chen, T. Xiao, X. Wang, Y. Qin, Z.L. Wang, Ultrathin piezotronic transistors with 2 nm channel lengths, ACS Nano 12 (2018) 4903-4908.

[27] X. Wang, X. He, H. Zhu, L. Sun, W. Fu, X. Wang, L.C. Hoong, H. Wang, Q. Zeng, W. Zhao, J. Wei, Z. Jin, Z. Shen, J. Liu, T. Zhang, Z. Liu, Subatomic deformation driven by vertical piezoelectricity from CdS ultrathin films, Sci. Adv. 2 (2016) e1600209-e1600209.

[28] R. Fei, W. Li, J. Li, L. Yang, Giant piezoelectricity of monolayer group IV monochalcogenides: SnSe, SnS, GeSe, and GeS, Appl. Phys. Lett. 107 (2015) 173104.

[29] H. Yin, J. Gao, G.-P. Zheng, Y. Wang, Y. Ma, Giant piezoelectric effects in monolayer group‐V binary compounds with honeycomb phases: a first-principles prediction, J. Phys. Chem. C 121 (2017) 25576-25584.

[30] G.-J. Lee, M.-K. Lee, J.-J. Park, D.Y. Hyeon, C.K. Jeong, K.-I. Park, Piezoelectric energy harvesting from two-dimensional boron nitride nanoflakes, ACS Appl. Mater. Interfaces 11 (2019) 37920-37926.

[31] Y. Li, Y. Rao, K.F. Mak, Y. You, S. Wang, C.R. Dean, T.F. Heinz, Probing symmetry properties of few-layer MoS_2 and h‐BN by optical second-harmonic

generation, Nano Lett. 13 (2013) 3329-3333.

[32]   Y. Zhou, D. Wu, Y. Zhu, Y. Cho, Q. He, X. Yang, K. Herrera, Z. Chu, Y. Han, M.C. Downer, H. Peng, K. Lai, Out-of-plane piezoelectricity and ferroelectricity in layered α^- In$_2$Se$_3$ nanoflakes, Nano Lett. 17 (2017) 5508-5513.

[33]   Y. Guo, S. Zhou, Y. Bai, J. Zhao, Enhanced piezoelectric effect in Janus group-III chalcogenide monolayers, Appl. Phys. Lett. 110 (2017) 163102.

[34]   Y. Wang, L.-M. Vu, T. Lu, C. Xu, Y. Liu, J.Z. Ou, Y. Li, Piezoelectric responses of mechanically exfoliated two-dimensional SnS$_2$ nanosheets, ACS Appl. Mater. Interfaces 12 (2020) 51662-51668.

[35]   P.-K. Yang, S.-A. Chou, C.-H. Hsu, R.J. Mathew, K.-H. Chiang, J.-Y. Yang, Y.-T. Chen, Tin disulfide piezoelectric nanogenerators for biomechanical energy harvesting and intelligent human-robot interface applications, Nano energy 75 (2020) 104879.

[36]   F. Liu, L. You, K.L. Seyler, X. Li, P. Yu, J. Lin, X. Wang, J. Zhou, H. Wang, H. He, S.T. Pantelides, W. Zhou, P. Sharma, X. Xu, P.M. Ajayan, J. Wang, Z. Liu, Room-temperature ferroelectricity in CuInP$_2$S$_6$ ultrathin flakes, Nat. Commun. 7 (2016) 12357-12357.

[37]   L. You, Y. Zhang, S. Zhou, A. Chaturvedi, S.A. Morris, F. Liu, L. Chang, D. Ichinose, H. Funakubo, W. Hu, T. Wu, Z. Liu, S. Dong, J. Wang, Origin of giant negative piezoelectricity in a layered van der Waals ferroelectric, Sci. Adv. 5 (2019) 3780-3780.

[38]   V. Maisonneuve, M. Evain, C. Payen, V.B. Cajipe, P. Molinié, Room-temperature crystal structure of the layered phase Cu^{I}In^{III}P$_2$S$_6$, J. Alloys Compd. 218 (1995) 157-164.

[39]   D.M. Kim, C.B. Eom, V. Nagarajan, J. Ouyang, R. Ramesh, V. Vaithyanathan, D.G. Schlom, Thickness dependence of structural and piezoelectric properties of epitaxial Pb(Zr$_{0.52}$Ti$_{0.48}$)O$_3$ films on Si and SrTiO$_3$ substrates, Appli. Phys. Lett. 88 (2006) 142904.

[40]   L. Lian, N.R. Sottos, Effects of thickness on the piezoelectric and dielectric properties of lead zirconate titanate thin films, J. Appl. Phys. 87 (2000) 3941-3949.

[41]   A.-Y. Lu, H. Zhu, J. Xiao, C.-P. Chuu, Y. Han, M.-H. Chiu, C.-C. Cheng, C.-W. Yang, K.-H. Wei, Y. Yang, Y. Wang, D. Sokaras, D. Nordlund, P. Yang, D.A. Muller, M.-Y. Chou, X. Zhang, L.-J. Li, Janus monolayers of transition metal dichalcogenides, Nat. Nanotechnol. 12 (2017) 744-749.

[42]   S. Liu, R.E. Cohen, Origin of negative longitudinal piezoelectric effect, Phys. Rev. Lett. 119 (2017) 207601-207601.

[43]   Y. Qi, A.M. Rappe, Widespread negative longitudinal piezoelectric responses in ferroelectric crystals with layered structures, Phys. Rev. Lett. 126 (2021) 217601-217601.

[44]   J.A. Brehm, S.M. Neumayer, L. Tao, A. O'Hara, M. Chyasnavichus, M.A. Susner, M.A. McGuire, S.V. Kalinin, S. Jesse, P. Ganesh, S.T. Pantelides, P. Maksymovych, N. Balke, Tunable quadruple-well ferroelectric van der Waals crystals, Nat. Mater. 19 (2020) 43-48.

[45]   S.M. Neumayer, E.A. Eliseev, M.A. Susner, A. Tselev, B.J. Rodriguez, J.A. Brehm, S.T. Pantelides, G. Panchapakesan, S. Jesse, S.V. Kalinin, M.A. McGuire, A.N. Morozovska, P. Maksymovych, N. Balke, Giant negative electrostriction and dielectric tunability in a van der Waals layered ferroelectric, Phys. Rev. Mat. 3 (2019) 024401.

[46]   L. Hu, X. Huang, Peculiar electronic, strong in-plane and out-of-plane second harmonic generation and piezoelectric properties of atom-thick α-M_2X_3 (M= Ga, In; X= S, Se): role of spontaneous electric dipole orientations, RSC Adv. 7 (2017) 55034-55043.

[47]   C.M. Lueng, H.L.W. Chan, C. Surya, C.L. Choy, Piezoelectric coefficient of aluminum nitride and gallium nitride, J. Appl. Phys. 88 (2000) 5360-5363.

[48]   I. Katsouras, K. Asadi, M. Li, T.B. van el, K.S. Kjaer, D. Zhao, T. Lenz, Y. Gu, P.M. Blom, g. Damjanovic, M.M. Nielsen, D.M. de Leeuw, The negative piezoelectric effect of the ferroelectric polymer poly(vinylidene fluoride), Nat. Mater. 15 (2016) 78-84.

[49]   J. Junquera, P. Ghosez, Critical thickness for ferroelectricity in perovskite ultrathin films, Nat. Mater. 422 (2003) 506-509.

[50]   Y. Liu, J. Guo, E. Zhu, L. Liao, S.-J. Lee, M. Ding, I. Shakir, V. Gambin, Y. Huang, X. Duan, Approaching the Schottky-Mott limit in van der Waals metal-semiconductor junctions, Nature 557 (2018) 696-700.

[51]   Y. Zhao, F. Guo, R. Ding, W.F. Io, S.Y. Pang, W. Wu, J. Hao, Piezo- phototronic effect in 2D α- In_2Se_3/WSe_2 van der Waals heterostructure for photodetector with enhanced photoresponse, Adv. Opt. Mater. 9 (2021) 2100864.

[52]   Z.L. Wang, W. Wu, Piezotronics and piezo-phototronics: fundamentals and applications, Natl. Sci. Rev. 1 (2014) 62-90.

[53]   Y. Liu, Y. Zhang, Q. Yang, S. Niu, Z.L. Wang, Fundamental theories of piezotronics and piezo-phototronics, Nano energy 14 (2015) 257-275.

[54]   W. Wu, C. Pan, Y. Zhang, X. Wen, Z.L. Wang, Piezotronics and piezo-phototronics – From single nanodevices to array of devices and then to integrated functional system, Nano today 8 (2013) 619-642.